

Geophysical Research Letters°



RESEARCH LETTER

10.1029/2021GL095287

Key Points:

- Passive high-resolution Vs imaging of shallow sedimentary layers with ocean-bottom distributed acoustic sensing and low-magnitude earthquakes
- Gridded slant-stack method to extract Scholte waves from local earthquake wavefields
- Full-wavefield simulations suggest that water phase reverberations generate Scholte waves at the ocean floor

Supporting Information:

Supporting Information may be found in the online version of this article.

Correspondence to:

Z. J. Spica, zspica@umich.edu

Citation:

Spica, Z. J., Castellanos, J. C., Viens, L., Nishida, K., Akuhara, T., Shinohara, M., & Yamada, T. (2022). Subsurface imaging with ocean-bottom distributed acoustic sensing and water phases reverberations. *Geophysical Research Letters*, 49, e2021GL095287. https://doi.org/10.1029/2021GL095287

Received 20 JUL 2021 Accepted 3 JAN 2022

Author Contributions:

Conceptualization: Zack J. Spica, Jorge C. Castellanos, Kiwamu Nishida Data curation: Zack J. Spica, Kiwamu Nishida, Takeshi Akuhara, Masanao Shinohara, Tomoaki Yamada Formal analysis: Zack J. Spica, Jorge C. Castellanos, Loïc Viens, Takeshi Akuhara Funding acquisition: Zack J. Spica, Masanao Shinohara, Tomoaki Yamada Investigation: Zack J. Spica, Jorge C. Castellanos, Kiwamu Nishida

© 2022. The Authors.
This is an open access article under the terms of the Creative Commons
Attribution-NonCommercial-NoDerivs
License, which permits use and distribution in any medium, provided the original work is properly cited, the use is non-commercial and no modifications or adaptations are made.

Subsurface Imaging With Ocean-Bottom Distributed Acoustic Sensing and Water Phases Reverberations

Zack J. Spica¹, Jorge C. Castellanos², Loïc Viens¹, Kiwamu Nishida³, Takeshi Akuhara³, Masanao Shinohara³, and Tomoaki Yamada³

¹Department of Earth and Environmental Sciences, University of Michigan, Ann Arbor, MI, USA, ²Department of Earth and Planetary Sciences, Seismological Laboratory, California Institute of Technology, Pasadena, CA, USA, ³Earthquake Research Institute, The University of Tokyo, Tokyo, Japan

Abstract Seismic waves from earthquakes recorded on the seafloor are composed of complex multiple arrivals. Here, distributed acoustic sensing (DAS) observations along a cable located offshore the Sanriku Coast, Japan, show that the local earthquake wavefield is particularly rich in Scholte waves. We introduce a processing pipeline to extract these surface waves from DAS records. We then invert hundreds of dispersion curves along a section of the cable to form a shallow high-resolution shear-wave velocity model. Moreover, we focus on the possible generation mechanisms of Scholte waves through a series of 2D and 3D full-wavefield numerical simulations. We show that water phase reverberations greatly contribute to the generation of Scholte waves on the ocean floor. This study demonstrates the potential of DAS to observe and better understand a poorly known marine wave phenomenon and image the offshore shallow seismic structure with an unprecedented spatial resolution.

Plain Language Summary Distributed acoustic sensing (DAS) is a measurement technique that has recently demonstrated its utility for marine geophysics. DAS offers the possibility to observe the seismic wave at a scale and an extent previously unattainable with traditional passive seismic surveys. Here, we use a linear DAS array located offshore the Sanriku Coast, Japan. We propose a processing pipeline to extract surface waves from local earthquake DAS records and obtain hundreds of measurements along the cable. These measurements are used to infer a high-resolution model of the near-shore subsurface. Supported by a series of numerical simulations, we suggest that acoustic reverberations in the water column greatly contribute to the generation of surface waves on the ocean floor. This study further demonstrates that DAS can be used to understand marine wave phenomena better and image offshore seismic structures.

1. Introduction

Our current knowledge of the near-shore shallow marine sediments greatly relies on sporadic core sampling and active seismic surveys conducted during expensive offshore campaigns. The characterization of marine sediments is of paramount importance for geotechnical engineering applications, seismic hazard assessment, and hydrocarbon exploration. Particularly, the determination of reliable shear-wave velocity (V_s) models is widely used for indirect evaluation of ground-motion amplification effects (Akal & Berkson, 2013; Sanchez-Sesma, 1987), sediment stability (Ayres & Theilen, 2001), and lithological variations and porosity (Hamilton, 1976). V_s models can be constructed using converted body and/or interface waves such as Scholte waves (Scholte, 1958). However, due to the weak P-to-S-wave conversion coefficient in shallow marine sediments, methods involving interface waves are often promoted (e.g., Bohlen et al., 2004; Kugler et al., 2007; Ritzwoller & Levshin, 2002).

Scholte waves can be directly excited by human (e.g., air-gun) and natural (e.g., earthquake) sources near the surface (e.g., Aki & Richards, 2002; Zhu & Popovics, 2006), or extracted from the ambient seismic noise (e.g., Mordret et al., 2013). Scholte waves can also be generated from water phase reverberations or by local body-wave scattering. Such interface waves generated from complex interactions between the ocean and the solid Earth have been recorded by offshore seismometers (Butler & Lomnitz, 2002; Tonegawa et al., 2015), but their generation mechanisms and their importance in oceanic seismic records are seldom reported in the literature.

Distributed acoustic sensing (DAS) recently became a powerful tool for seismologists (Lindsey & Martin, 2020; Zhan, 2020). This interferometric laser-based technology allows geophysicists to turn fiber-optic cables into thousands of seismic sensors spaced by a few meters (Grattan & Sun, 2000; Posey et al., 2000). The high density of

SPICA ET AL.



Methodology: Zack J. Spica, Jorge C. Castellanos, Loïc Viens Project Administration: Takeshi Akuhara, Masanao Shinohara, Tomoaki Yamada

Resources: Zack J. Spica, Kiwamu Nishida, Takeshi Akuhara, Masanao Shinohara, Tomoaki Yamada Software: Zack J. Spica, Jorge C. Castellanos

Validation: Zack J. Spica, Jorge C. Castellanos, Kiwamu Nishida Writing – original draft: Zack J. Spica, Loïc Viens DAS records offers the possibility to study the seismic wavefield with a spatial resolution and an extent previously unattainable with traditional passive seismic surveys (e.g., Lellouch et al., 2019). Moreover, recent underwater experiments demonstrated that DAS can register high-fidelity wavefield, setting it as a new high-density seismo-acoustic measurement method for marine geophysics (Ide et al., 2021; Lindsey et al., 2019; Lior et al., 2021; Matsumoto et al., 2021; Rivet et al., 2021; Sladen et al., 2019; Williams et al., 2019) and offshore seismic imaging (Cheng et al., 2021; Spica, Nishida, et al., 2020; Taweesintananon et al., 2021; Williams et al., 2021).

In this study, we show that ocean-bottom DAS seismic records of local earthquakes are particularly rich in Scholte waves. Using a DAS cable offshore the Sanriku Coast, Japan (Figure 1, M. Shinohara, T. Yamada, Akuhara et al., 2019), we develop a method to search and extract dispersive features from several low-magnitude earthquakes. We obtain hundreds of dispersion curves (DC) that we invert to construct a 2D high-resolution V_s model of the shallow subsurface that shows strong lateral and vertical heterogeneities. In addition, we introduce a series of 2D and 3D full-wavefield simulations to understand the generation mechanisms of Scholte waves on the ocean floor. These simulations help us to understand under which conditions and assumptions our imaging scheme provide accurate estimation of the Scholte waves' phase velocity.

2. Data

The fiber-optic cable sustains an ocean-bottom seismometer and tsunami-meter array (Figure 1; Kanazawa & Hasegawa, 1997; M. Shinohara, T. Yamada, Sakai et al., 2016). This 115 km cable is perpendicular to the coast and buried under shallow sediments for the first ~48 km. Two DAS measurement campaigns were conducted in 2019 (from February 13 to 15 and from November 18 to December 2) with an AP Sensing N5200A interrogator (Cedilnik et al., 2019). For both campaigns, the parameters of the interrogator were set to record strain with a 5 m channel spacing, a 40 m gauge length, and a 500 Hz sampling frequency. In this contribution, we focus on the first 10 km of the cable, where we observe a high signal-to-noise ratio (SNR) for earthquakes and where the topography is the most horizontal (Figure 1b). We only analyze earthquakes with a SNR ≥10 and at a maximum distance of ~150 km from the cable (Supporting Information S1). More details about the cable setup and measurement quality can be found in M. Shinohara, T. Yamada, Akuhara, et al. (2019) and Spica, Nishida, et al. (2020).

3. Scholte Waves in Earthquake Wavefields

Figure 2a shows the wavefield generated by a moderate Japan Meteorological Agency velocity magnitude (M_V) 3.0 earthquake (#1 in Figure 1). The direct P-wave arrival is very weak in this example, which can be explained by a lower sensitivity of DAS to a quasi-vertically incident wavefield perpendicular to the cable (Martin et al., 2018). However, the direct S-wave appears clearly in the DAS record due to its higher sensitivity along the cable (Figures 2a and 2f). Figure S1 in the Supporting Information S1 shows another example of a DAS wavefield for a M_V 2.5 earthquake with a clearer P wave (#2 in Figure 1). For both earthquakes, we identify several low-velocity surface-wave packets with relatively high amplitude and clear dispersive features after the direct S-wave arrival. These surface waves appear almost everywhere along the DAS record segment and travel both landward and seaward. However, their SNR is highly variable, which could be explained by complex interactions with the shallow structure that locally deteriorate or amplify the signal (e.g., Lior et al., 2021; van den Ende & Ampuero, 2021), or some differences in the coupling of the cable.

We develop a gridded slant-stack (GSS) method to detect coherent surface-wave energy in the DAS wavefields. Within this framework, we band-pass filter earthquake wavefields in the time domain using a cascade of narrow-band Gaussian filters and scan the entire record sections to search for coherent dispersive features. For each of the record sections, we use a 2D running window with a 90% overlap that is 830 m wide in space and 1.96 s in time. The 830 m spacial window corresponds to the longest wavelength observed in the targeted frequency range. We derived this number from a reference synthetic DC from Spica, Nishida, et al. (2020). The 1.96 s was set to allow at least 4 wavelengths in the time window to avoid any potential aliasing. We then perform a slant-stack analysis for each window, where we shift-and-stack the filtered waveforms to search for the phase velocity that results in the most coherent output. Here, we limit this search to a ±50% velocity anomaly from the reference DC. We perform this calculation individually for 15 period bands, which are linearly spaced between 0.2 and 1 s, for both landward and seaward wave propagation directions. The results are then stacked in the frequency dimension to provide a marker in distance and time where there is coherent and dispersive energy in the DAS wavefield. The

SPICA ET AL. 2 of 11

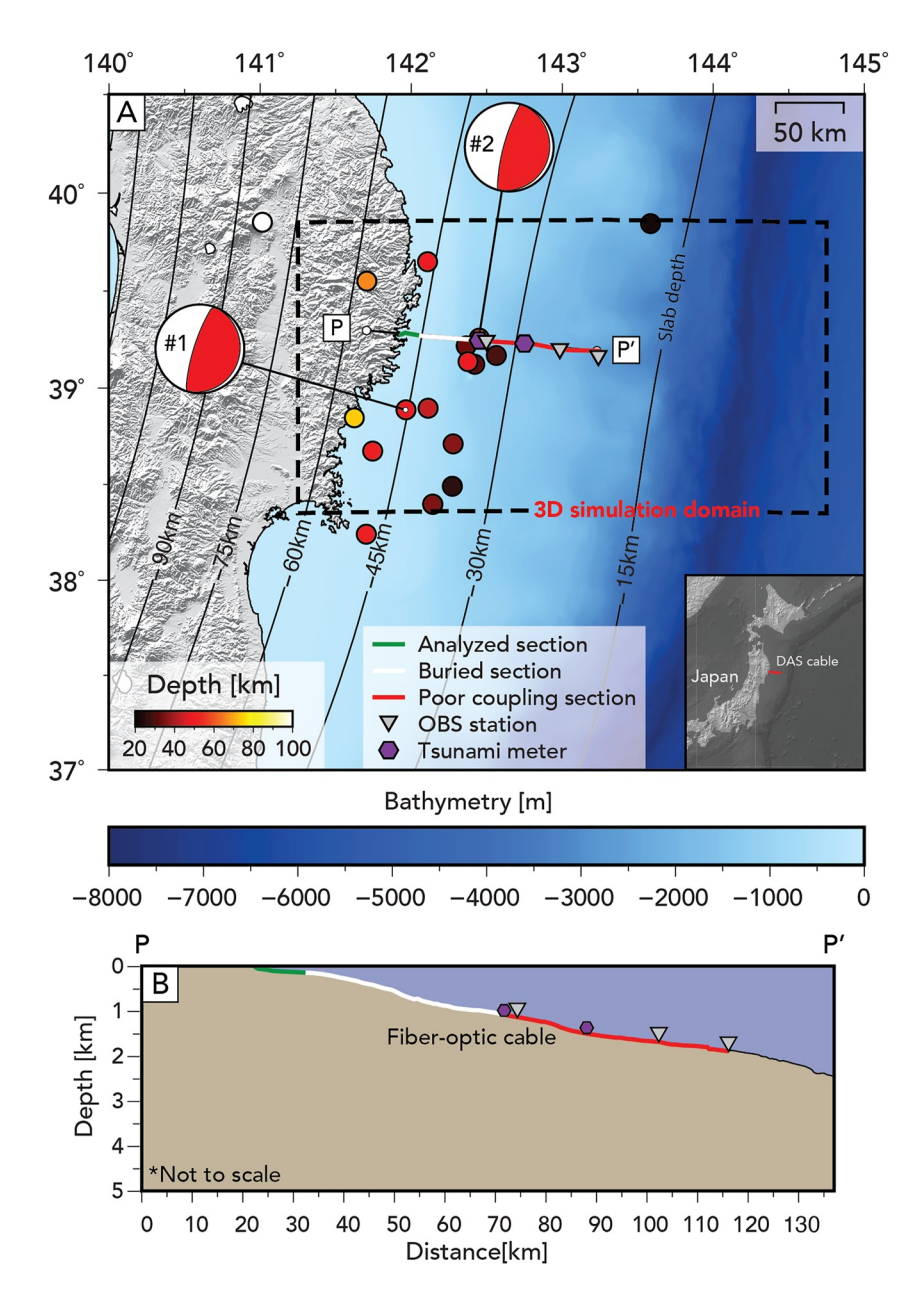


Figure 1. (a) Map of the fiber-optic cable offshore the coast of Sanriku, Japan. The green and white sections of the cable are buried in shallow sediments and the red section lies directly on the ocean floor. The colored circles depict the 18 earthquakes used in this study. The earthquakes highlighted with moment tensor solutions are #1: 2019-02-14T21:10:50 UTC and #2: 2019-11-20T21:38:05 UTC, occurred at 49 and 50 km depth, and are of magnitude M_V 3.0 and 2.5, respectively. (b) Bathymetry profile between P and P'.

output of the GSS shown in Figures 2b and 2c is a heatmap representing the stack of all computed frequencies. It highlights regions of the seismic wavefield where surface waves share standard features (i.e., velocity and frequency content). The GSS detections for the earthquake #2 are shown in Figure S1 in the Supporting Information S1, and we repeat the GSS process for 18 earthquakes with M_V ranging between 1.6 and 3.5.

Theoretically, if the GSS are computed at a higher sampling frequency, we could extract DCs directly from these measurements. However, due to the heavy computational load involved, we add a supplementary (but fastest) step to extract the dispersive features from the record sections. We automatically extract the Scholte wave packets using constant windows of 830 m and 1.96 s, centered on the maximum energies detected by the stacked GSS. Figure 2g shows an example of an extracted window with surface waves traveling at about 660 m/s. In total, we

SPICA ET AL. 3 of 11

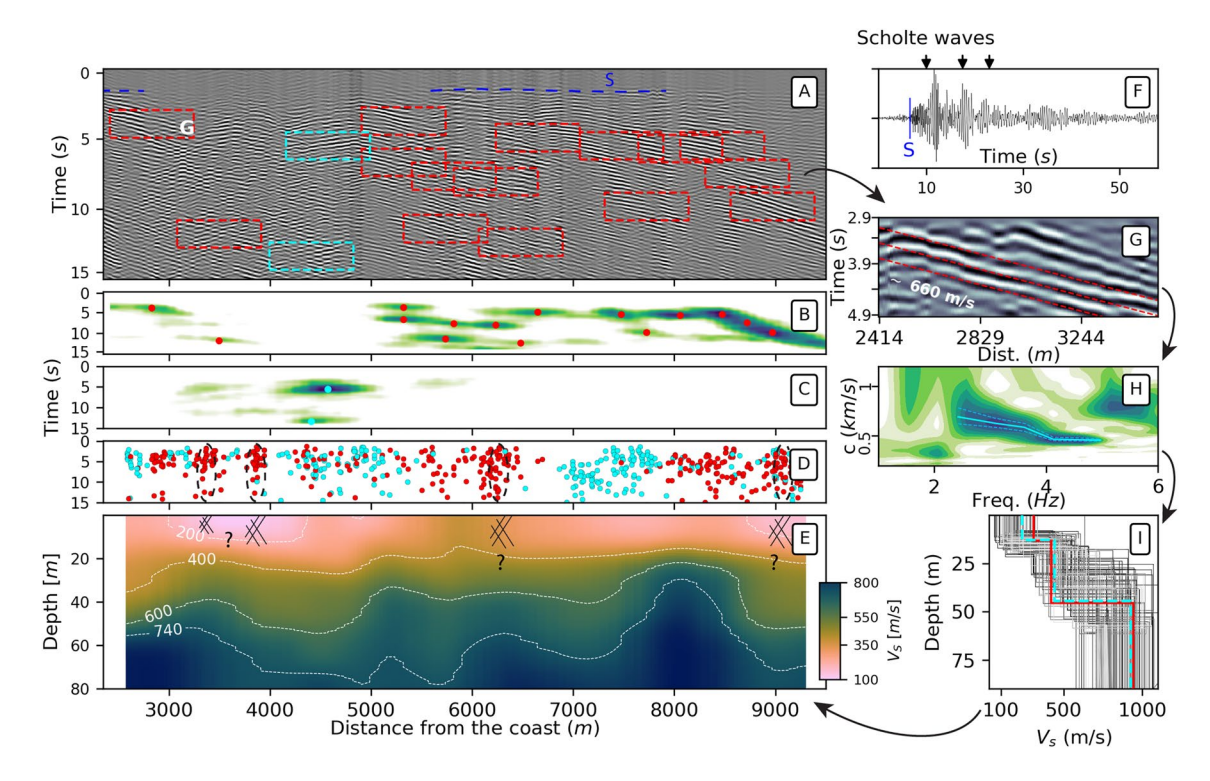


Figure 2. (a) Distributed acoustic sensing (DAS) earthquake wavefield filtered between 0.5 and 8 Hz for earthquake #1. The dashed blue line depicts the direct *S*-wave arrival. The rectangular boxes show the selected gridded slant-stack (GSS) windows used to extract surface-wave energies. In all panels, the red and cyan colors correspond to seaward and landward propagations, respectively. (b) Stacked GSS result for seaward propagation. (c) Same as (b) for landward propagation. In (b and c), the dots depict the maximum GSS power, which is the center of the extraction windows in (a). (d) All the Scholte-wave energies detected after the *S*-wave using the GSS for the 18 earthquakes. The dashed ellipses highlight a higher concentration of seaward detection. (e) Smoothed inverted 2D velocity model. The question marks depict regions of higher scattering and/or surface wave amplification. (f) Example of a single DAS seismogram extracted from panel (a) at channel 500, 2,500 m from the coast. (g) Zoom in the upper left red window extracted from panel (a). (h) Dispersion image obtained using the windowed signal in (g). (i) 1D velocity model obtained using the dispersion curves in (h).

identify 609 Scholte wave packets (346 seaward and 263 landward) from 18 earthquakes unevenly distributed along the first 10 km of the cable. Their arrival times are shown in Figure 2d, where we observe a region with no seaward detection (between 6,500 and 8,000 m from the coast) and other regions with more detections.

3.1. 2D *V_s* Model

We apply a Tukey-window time filter to all the extracted Scholte-wave windows to mute arrivals slower than 150 m/s and faster than 1,000 m/s. All the extracted Scholte waves from earthquake #1 are shown in Figure S2 in the Supporting Information S1. We then calculate Scholte wave phase dispersion images via a $\tau - p$ transform (Figure S3 in the Supporting Information S1; McMechan & Yedlin, 1981). About 9% of all the dispersion images show poor coherency (i.e., no continuous dispersion for less than 1/4 wavelength of the extracted window) and are automatically rejected (e.g., station at 6,230 m in Figure S3 in the Supporting Information S1). Approximately 16% of the dispersion images are stacked together when two or more surface-wave packets are detected for the same region (e.g., station at 5,318 m in Figure S3 in the Supporting Information S1). This process yields more stable measurements (e.g., Spica, Perton, et al., 2020; Yuan et al., 2020) with average velocities for a given region. After rejection and stacking, we obtain a total of 482 DCs unevenly distributed along the cable and showing reliable estimates of the phase velocity between ~1 Hz and 7 Hz.

We invert the DCs following the method described in Spica, Perton, et al. (2020). The inversion was performed for the thickness and V_s of two layers overlying a half-space. Examples of inverted DCs and 1D V_s models extracted from earthquake #1 are shown in Figures S4 and S5 in the Supporting Information S1, respectively. The final 2D velocity profile (Figure 2e) is constructed by averaging all the 1D models into distance bins of 70 m and applying a locally weighted 2D smoothing (Cleveland, 1979). For comparison, Figure S6 in the Supporting

SPICA ET AL. 4 of 11



Information S1 shows the unsmoothed 2D velocity model along with the one standard deviation (1σ) from the averaged binned profile, the V_S30 , and a histogram of the number of profiles averaged for each region, as well as the dissimilarity between landward and seaward velocity models. These alternative models allow to assess better small-scale heterogeneities supported by multiple inversion results. Figure S7 in the Supporting Information S1 shows all the individual velocity models obtained in this study.

As expected, we observe a significant degree of V_s spatial variability, especially at shallow depth (\sim 15 m below seabed) with velocities under 150 m/s. Such low velocities in the first tens of meters may suggest that the sediments are subjected to a low effective stress with a porosity close to the suspension limit. The maximum lateral variation is found near 6,200 m from the coast, where the topmost velocity sharply decreases by about 50% from \sim 500 to \sim 250 m/s. Interestingly, a higher number of GSS seaward detections is found in low-velocity and contrasting-velocity regions. This implies that the velocity model is better constrained in these areas but also suggests a structural control on the generation of Scholte waves. Accordingly, such seaward propagating surface waves could be reflected waves from strong lateral heterogeneities or locally amplified waves due to strong impedance contrast at depth. The underlying sedimentary layers are also characterized by a strong vertical gradient, sometimes higher than 100% on a 50 m depth interval (e.g., at \sim 20 m depth near 8,000 m from the coast).

Although the waves used to construct the velocity model have evident dispersive features, it is unclear why they are so abundant in the earthquake records. In the next section, we present a series of simulations to explain the possible generation mechanisms of such dispersive waves.

4. Full-Wavefield Simulations

Figure 3 and Videos v1–3 (in the Movies S1–S3) show the results from a series of 2D finite-difference simulations (Li et al., 2014) with a two-domain (i.e., fluid and solid) velocity model that incorporates a realistic bathymetry profile (Figure S8a in the Supporting Information S1; NOAA, 2009). Figure 3a, depicts three different scenarios. In a first simulation (scenario A), we set a free surface condition on top of the water layer. In a second simulation (scenario B), we use the same configuration as in scenario A, but we set an absorbing boundary condition on top of the water layer. The third scenario (C) corresponds to the subtraction of simulation B from simulation A. By doing so, we remove the wave phenomena that occur in the solid Earth and highlight the contribution from the water column. Scenario C in Figure 3b reveals that a significant part of the seismic energy that is seen in scenario A originates from interactions between water (acoustic) phases and the ocean floor.

Theoretically, water phases can be excited by both P- and S-waves and travel with different slopes in the water layer (e.g., pw_n and sw_n in Figure 3b). Here, w stands for the acoustic waves in the water layer and n denotes phases related to the nth water surface reflection. These water phases can either propagate laterally in the water column (e.g., T-phase; Kosuga, 2011; Okal, 2008; Talandier & Okal, 1998) or be efficiently converted back into elastic energy in the solid Earth. In the latter case, water phases can bounce back and forth between the ocean surface and bottom, and successive reflections promote the generation of a modified wavefront with vertical propagation, which eventually forms a standing wave (Yue et al., 2017) that can last for tens of seconds. When the water wavefront is normal to the ocean bottom interface, the acoustic/elastic conversion coefficient is maximal, and refracted acoustic phases generate curved P wavefronts (pw_nP and sw_nP). These acoustic pulses are followed by disturbances that spread over the seafloor in the form of symmetrical annular wave systems with surface-wave velocities.

Figure 3c show the synthetic seismograms as they would be recorded by a near-shore ocean-bottom DAS (Figure S8a in the Supporting Information S1) for scenarios A and C. In scenario C, we observe several linear arrivals with velocities around 2.5 km/s (i.e., the shallow shear-wave velocity) that arrive at regular intervals after the direct P- (with low amplitude) and S-wave (with slightly higher amplitude). These surface waves are generated everywhere along the synthetic DAS array and travel both landward and seaward. They show higher amplitudes on the western side of the array where the bathymetry tends to be more horizontal, promoting the generation of standing waves with orthogonal incidence and, therefore, a possible higher conversion rate. See Supporting Information and Figure S9 in the Supporting Information S1 for synthetic seismograms accounting for shallow low-velocity layers (Koketsu et al., 2012).

SPICA ET AL. 5 of 11



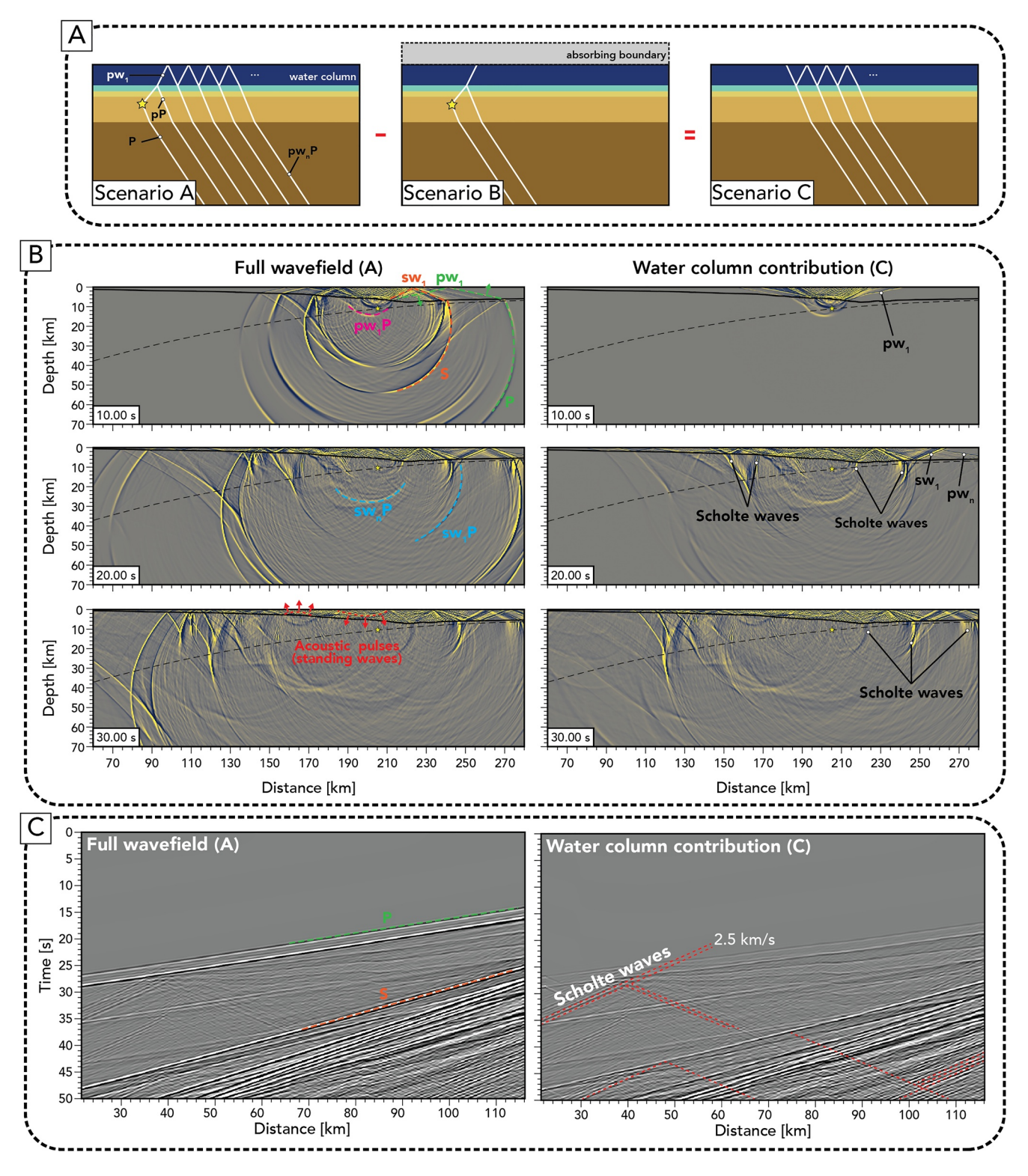


Figure 3. (a) Schematic diagrams showing the ray paths of the direct P-wave, the depth phases (pP), and the first four water multiples (pw_nP) for the three different scenarios. (b) Snapshots of 2D velocity wavefield (v_{xx}) at different time steps. The full-wavefield depicts the scenario A while the water column contribution depicts the scenario C. The full videos showing the three different scenarios are available in the Movie S1–S5. (c) 2D waveform modeling results along a synthetic distributed acoustic sensing array. The green and orange dashed lines depict the P and S wavefronts, while the red dashed lines depict surface waves packet along the array.

SPICA ET AL. 6 of 11



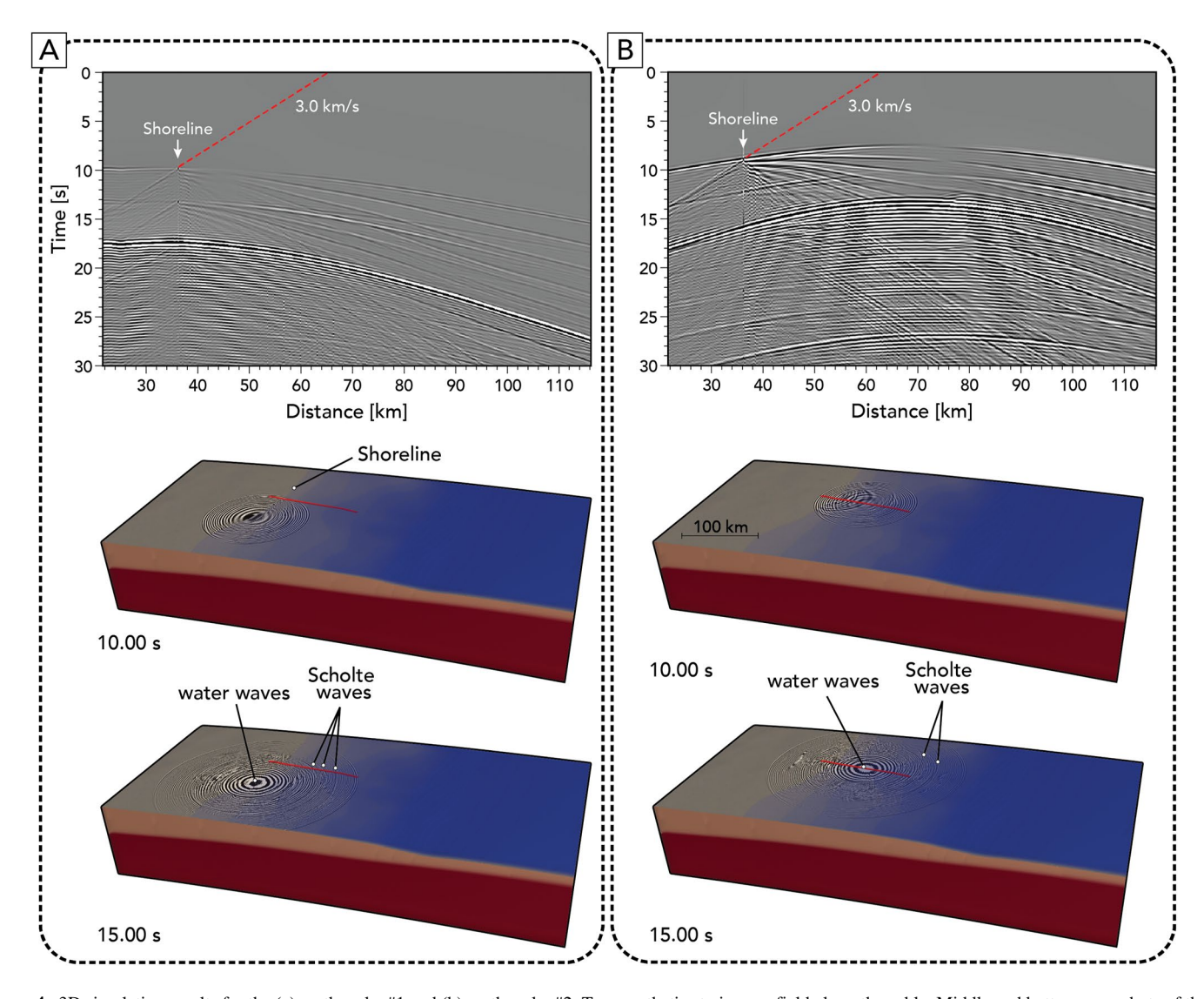


Figure 4. 3D simulation results for the (a) earthquake #1 and (b) earthquake #2. Top: synthetic strain wavefield along the cable. Middle and bottom: snapshots of the 3D wavefields at different times.

These simulations demonstrate that under the smooth geometry of the simulation domain, strong water phases can significantly contribute to the generation of Scholte waves on the ocean floor. It is worth noting that in addition to the geometry of the continental slope, the degree of roughness of the simulation model could also plays a leading role in the generation of water phases.

Regardless of the generation mechanism, the processing to extract and invert Scholte waves from the earthquake wavefield is valid under the sole condition that these waves travel parallel to the cable to ensure an optimal phase velocity estimation; however, the 2D modeling does not guarantee that Scholte waves travel parallel to the cable when a source is shifted from the cable axis. Therefore, we perform fully coupled 3D numerical simulations for two scenarios to test the effect of off-azimuth propagation on the estimation of local phase velocities (Figure S8b in the Supporting Information S1, Videos v4–v5 in the Movies S4 and S5). In Figure 4a, the source is shifted about 50 km south of the cable to mimic the location of the earthquake #1. In Figure 4b, the source is located directly beneath the DAS array as for the earthquake #2. In both simulations, we incorporate the water layer, a realistic smooth bathymetric model (Hirt & Rexer, 2015), and a Moho topography model (Laske et al., 2013). We then calculate the earthquake-induced strain at the ocean floor using a high-performance spectral-element solver (Afanasiev et al., 2019). The top panels in Figure 4 show the synthetic E-W strain that is obtained from the two scenarios. We observe that both sets of recordings display several hyperbolic arrivals that correspond to direct

SPICA ET AL. 7 of 11



body waves and converted waves generated by acoustic reverberations. Moreover, we note several linear arrivals that travel with an average velocity of 3.0 km/s, which is the shear-wave velocity assigned to the shallow crust in the 3D synthetic domain. These arrivals are Scholte and surface waves propagating at the solid-fluid and solid-air interfaces (depending on whether the receivers are located on the seafloor or at the free-surface), respectively. Therefore, regardless of the earthquake source location, the origin of these wave packets is the shoreline, which is, for all practical purposes, the only prominent scatter point within the simulation domain.

These results support the hypothesis that even if the earthquake source is not in direct alignment with the cable, both direct body waves and continuous water phases can excite several parallel-to-cable propagating Scholte waves as long as there is a major scatter point along the cable. It also sheds light on the possible generation mechanism of these waves in the DAS records.

5. Discussion

5.1. Reliability of the V_S Model

To evaluate the stability of the main V_S model in Figure 2e, we present an estimation of the model stability (1σ) along with a series of alternative models obtained using only inversion results from earthquakes aligned with the cable and using only landward versus seaward Scholte waves (Figure S6 in the Supporting Information S1). In addition, we compute the percentage of velocity change between these alternative models and the main model. The standard deviation of velocity between individuals models for each bin is relatively large in the deep and western areas, and overall, absolute velocities in the main model appear to be better constrained at shallow depths (Figure S6d in the Supporting Information S1). All the alternative models reproduce the same features of the main model, suggesting that most of the surface waves extracted from our processing share similar properties for a given bin. This also indirectly suggests that the location of the source and the possible different generation mechanisms of Scholte waves have a negligible impact on the final velocity model. However, we observe larger dissimilarities in the western part of the models and almost everywhere around 20 m depth. As all the 1D models are constructed with two layers overlying a half-space, these local dissimilarities result from changes in interface depths rather than flawed estimations of the absolute velocities. This is because DCs are sensitive to absolute velocity variation with depth but are only weakly sensitive to the details of the layering (e.g., Spica et al., 2018). Also, we can expect the velocity models to offer only a smooth representation of the actual velocity structure because the DCs are expressed across small subarrays of 830 m and then arbitrarily averaged into 70 m bins. This averaging process tends to reduce possible errors on the likely imperfect estimation of the velocity due to nonparallel Scholte wave propagation. Finally, because we used data from two different measurement campaigns, we expect that the medium has not changed and has not been affected by regional seismicity between measurements.

5.2. Understanding Near-Coast Scholte Waves Generation

Based on a series of observations and simulations, we show that water phases play a leading role in the generation of Scholte waves on the ocean floor. After an earthquake occurs, a portion of the seismic waves is transmitted into the water body and converted into acoustic waves. Such phases propagate in 3D and radially from the source (i.e., the conversion point) into the water, where attenuation is remarkably low. The quasi non-attenuation of acoustic waves implies that successive reflections between the ocean surface and bottom can efficiently promote a re-conversion into elastic energy. Theoretically, an orthogonal acoustic ray could be seen as a normal force on the seafloor for which about 75% of the refracted energy can be converted into surface waves that propagate along the free surface (Lamb, 1904). In the simulations, the effective coupling between acoustic and Scholte waves is ensured by the high shear-wave velocity of the crust near the ocean bottom (~2,500 m/s, Figure S8 in the Supporting Information S1). In reality, however, the shallow sediments have extremely low velocities (Figure 2e), which implies that the difference in phase velocity between acoustic and Scholte waves is too large to guarantee an efficient coupling of the waves and thus an effective conversion. Therefore, we suggest a possible alternative mechanism. After an acoustic ray reverberates in the near-vertical direction, the acoustic energy is gradually partitioned into S-waves. The low velocity of the sediments favors the trapping of S-waves, which reverberate inside the shallow sedimentary layers as suggested by Spica, Nishida, et al. (2020). The complex sedimentary structure tends to increasingly homogenize the waves' incident angle, which gradually leads to energy leaks in the

SPICA ET AL. 8 of 11



horizontal direction. Such horizontally propagating waves are the observed Scholte waves, arriving at different times along a cable segment.

Aside from the water reverberation excitation, Scholte waves can also be generated locally through body-wave scattering at sharp bathymetric features (Zheng et al., 2013) or at strong lateral heterogeneities such as fault zones (Sato et al., 2012). In addition, the intrinsic nature of DAS, which measures strain rather than particle motion, makes it more sensitive to local heterogeneities (Singh et al., 2020). Therefore, it is very likely that in addition to water phase reverberations, localized scattering, and amplification also contribute to the generation of Scholte waves along the cable. As a heterogeneity is practically a scatter point anchored in the subsurface, scattered Scholte waves should be observed as persistent and localized features in most earthquake DAS records. Contrastingly, acoustically generated Scholte waves should be observed irregularly along the cable, as their generation mostly depends on the complex geometry between the source, the conversion point, and the bathymetry. Figure 2d shows that most of the extracted Scholte waves occurred unevenly along the cable, which supports our main hypothesis. Nonetheless, we also observe at least four regions where most earthquakes repeatedly generate coherent Scholte waves. One of these regions (e.g., near 6,200 m from the coast in Figure 4e) was previously identified as a potential unmapped fault zone using reflection image from autocorrelations of ambient seismic noise (Spica, Nishida, et al., 2020). In the new velocity model, this area corresponds to a strong shallow horizontal velocity contrast. In the 2D case, most of the surface-wave energy would radiate out from the scatter point as a symmetrical semi-circular wave system in the opposite direction of the incident waves (Chai et al., 2012), which should guarantee a proper estimation of the phase velocity along the cable. In 3D, however, the heterogeneity could be slightly offset from the cable leading to an inaccurate estimation of the phase velocity in this area. The three other regions with higher measurement density correspond to shallow low-velocity areas. Because DAS measures ground motion gradients, the wave amplitudes are inversely proportional to the apparent phase velocity. Therefore, slow waves in shallow sediments are amplified in the DAS records (e.g., van den Ende & Ampuero, 2021). This phenomenon may be exacerbated by the extreme low velocities observed in these areas.

6. Conclusion

The conclusion of this study are twofold. (a) We proposed a data processing pipeline to extract and invert surface-wave packets recorded by an ocean-bottom DAS array. We showed that it is possible to passively use DAS cable and local seismicity to generate a high-resolution 2D V_s velocity model that is important for near-shore exploration and ground-motion prediction. (b) We used state-of-the-art simulation methods along with observations to better understand the wave phenomena promoting the generation of Scholte waves on the seafloor. We suggest that an important fraction of the Scholte wave energy in earthquake records can originate from complex interactions between acoustic and seismic phases. Importantly, this assumption only holds under the geometrical configuration of this study (i.e., a cable perpendicular to the shore on top of a relatively steep bathymetry), and should be therefore further tested for different cable settings.

Our new passive approach is an alternative to ambient seismic noise correlation methods to image the shallow offshore subsurface. In addition, as the fiber-optic cable is a passive component that can be left on the ocean floor for a virtually unlimited amount of time, the method is non-invasive, does not require a dedicated survey, can be used to extract V_s profiles directly, and can be repeated at different times at almost no additional cost. Furthermore, we demonstrate the possibility of using low-magnitude earthquakes for shallow imaging, suggesting that this method could be readily exported to other seismically active regions worldwide where fiber-optic telecommunication cables lie on the seafloor.

Conflict of Interest

The authors declare no conflicts of interest relevant to this study.

Data Availability Statement

All the data necessary to reproduce the results presented in the paper (e.g., earthquakes #1 & #2) are open access and available at https://doi.org/10.5281/zenodo.5110823. The Gridded Slant-Stack code is available for download on GitHub (https://github.com/zackspica/Gridded-SlantStack) with https://doi.org/10.5281/zenodo.5608598.

SPICA ET AL. 9 of 11



Acknowledgments

We thank Fujitsu for cooperating with the Earthquake Research Institute (ERI), the University of Tokyo, for the DAS measurement campaigns. All the figures have been plotted with Matplotlib (Hunter, 2007) or the Generic Mapping Tool (Wessel et al., 2019). Some of the data processing steps have been performed using ObsPy (Beyreuther et al., 2010), and Pyrocko (Heimann et al., 2017). We thank Michael Afanasiev and the Mondaic team for their help in setting up the 3D numeric simulations. This project was partly supported by the discretionary budget of the director of ERI. The observations were carried out as part of the Earthquake and Volcano Hazards Observation and Research Program by the Ministry of Education, Culture, Sports, Science, and Technology of Japan. Z.J.S thanks the Air Force Research Laboratory through project FA9453-21-2-0018. L.V was supported by NSF award EAR2022716, and J.C.C. was supported by NSF CAREER award 1848166 and the Gordon and Betty Moore Foundation. The authors wish to thank the editor Daoyuan Sun, and two anonymous referees for their reviews that helped to improve the quality of the paper and the interpretation of the results.

References

- Afanasiev, M., Boehm, C., van Driel, M., Krischer, L., Rietmann, M., May, D. A., et al. (2019). Modular and flexible spectral-element waveform modelling in two and three dimensions. *Geophysical Journal International*, 216(3), 1675–1692. https://doi.org/10.1093/gji/ggy469
- Akal, T., & Berkson, J. M. (2013). Ocean seismo-acoustics: Low-frequency underwater acoustics (Vol. 16). Springer Science & Business Media. Aki, K., & Richards, P. (2002). Quantitative seismology. University Science Book.
- Ayres, A., & Theilen, F. (2001). Relationship between P-and S-wave velocities and geological properties of near-surface sediments of the continental slope of the Barents Sea. *Geophysical Prospecting*, 47(4), 431–441. https://doi.org/10.1046/j.1365-2478.1999.00129.x
- Beyreuther, M., Barsch, R., Krischer, L., Megies, T., Behr, Y., & Wassermann, J. (2010). ObsPy: A Python toolbox for seismology. Seismological Research Letters, 81(3), 530–533. https://doi.org/10.1785/gssrl.81.3.530
- Bohlen, T., Kugler, S., Klein, G., & Theilen, F. (2004). 1.5 D inversion of lateral variation of Scholte-wave dispersion. *Geophysics*, 69(2), 330–344. https://doi.org/10.1190/1.1707052
- Butler, R., & Lomnitz, C. (2002). Coupled seismoacoustic modes on the seafloor. *Geophysical Research Letters*, 29(10), 57–61. https://doi.org/10.1029/2002g1014722
- Cedilnik, G., Lees, G., Schmidt, P., Herstrøm, S., & Geisler, T. (2019). Ultra-long reach fiber distributed acoustic sensing for power cable monitoring. In *Proceedings of the JICABLE*.
- Chai, H. Y., Phoon, K. K., Goh, S. H., & Wei, C. F. (2012). Some theoretical and numerical observations on scattering of Rayleigh waves in media containing shallow rectangular cavities. *Journal of Applied Geophysics*, 83, 107–119. https://doi.org/10.1016/j.jappgeo.2012.05.005
- Cheng, F., Chi, B., Lindsey, N. J., Dawe, T. C., & Ajo-Franklin, J. B. (2021). Utilizing distributed acoustic sensing and ocean bottom fiber optic cables for submarine structural characterization. *Scientific Reports*, 11(1), 1–14. https://doi.org/10.1038/s41598-021-84845-y
- Cleveland, W. (1979). Robust locally weighted regression and smoothing scatterplots. *Journal of the American Statistical Association*, 368(74), 829–836. Taylor & Francis. https://doi.org/10.1080/01621459.1979.10481038
- Grattan, K., & Sun, T. (2000). Fiber optic sensor technology: An overview. Sensors and Actuators A: Physical, 82(1-3), 40-61. https://doi.org/10.1016/s0924-4247(99)00368-4
- Hamilton, E. L. (1976). Shear-wave velocity versus depth in marine sediments: A review. Geophysics, 41(5), 985–996. https://doi.org/10.1190/1.1440676
- Heimann, S., Kriegerowski, M., Isken, M., Cesca, S., Daout, S., Grigoli, F., et al. (2017). Pyrocko An open-source seismology toolbox and library. GFZ Data Services.
- Hirt, C., & Rexer, M. (2015). Earth2014: 1 arc-min shape, topography, bedrock and ice-sheet models—available as gridded data and degree-10,800 spherical harmonics. *International Journal of Applied Earth Observation and Geoinformation*, 39, 103–112. https://doi.org/10.1016/j.
- Hunter, J. D. (2007). Matplotlib: A 2D graphics environment. Computing in Science & Engineering, 9(3), 90–95. https://doi.org/10.1109/mcse.2007.55
- Ide, S., Araki, E., & Matsumoto, H. (2021). Very broadband strain-rate measurements along a submarine fiber-optic cable off cape muroto, nankai subduction zone, Japan. Earth, Planets and Space, 73(1), 1–10. https://doi.org/10.1186/s40623-021-01385-5
- Kanazawa, T., & Hasegawa, A. (1997). Ocean-bottom observatory for earthquakes and tsunami off Sanriku, north-east Japan using submarine cable, paper presented at international workshop on scientific use of submarine cables, comm. for sci. Use of Submarine Cables.
- Koketsu, K., Miyake, H., & Suzuki, H. (2012). Japan integrated velocity structure model version 1. In *Proceedings of the 15th World conference on earthquake engineering* (p. 1773).
- Kosuga, M. (2011). Localization of t-wave energy on land revealed by a dense seismic network in Japan. *Geophysical Journal International*, 187(1), 338–354. https://doi.org/10.1111/j.1365-246x.2011.05143.x
- Kugler, S., Bohlen, T., Forbriger, T., Bussat, S., & Klein, G. (2007). Scholte-wave tomography for shallow-water marine sediments. Geophysical Journal International, 168(2), 551–570. https://doi.org/10.1111/j.1365-246x.2006.03233.x
- Lamb, H. (1904). I. on the propagation of tremors over the surface of an elastic solid. Philosophical Transactions of the Royal Society of London -Series A: Containing Papers of a Mathematical or Physical Character, 203(359–371), 1–42.
- Laske, G., Masters, G., Ma, Z., & Pasyanos, M. (2013). Update on CRUST1. 0-A 1-degree global model of Earth's crust. Geophysical Research Abstracts. 15, 2658.
- Lellouch, A., Yuan, S., Spica, Z., Biondi, B., & Ellsworth, W. L. (2019). Seismic velocity estimation using passive downhole distributed acoustic sensing records: Examples from the San Andreas fault observatory at depth. *Journal of Geophysical Research: Solid Earth*, 124(7), 6931–6948. https://doi.org/10.1029/2019JB017533
- Li, D., Helmberger, D., Clayton, R. W., & Sun, D. (2014). Global synthetic seismograms using a 2-D finite-difference method. *Geophysical Journal International*, 197(2), 1166–1183. https://doi.org/10.1093/gji/ggu050
- Lindsey, N. J., Dawe, T. C., & Ajo-Franklin, J. B. (2019). Illuminating seafloor faults and ocean dynamics with dark fiber distributed acoustic sensing. Science, 366(6469), 1103–1107. https://doi.org/10.1126/science.aay5881
- Lindsey, N. J., & Martin, E. R. (2021). Fiber-Optic Seismology. Annual Review of Earth and Planetary Sciences, 49, 309–336. https://doi.org/10.1146/annurev-earth-072420-065213
- Lior, I., Sladen, A., Rivet, D., Ampuero, J. P., Hello, Y., Becerril, C., et al. (2021). On the detection capabilities of underwater distributed acoustic sensing. *Journal of Geophysical Research: Solid Earth*, 126(3), e2020JB020925. https://doi.org/10.1029/2020jb020925
- Martin, E. R., Lindsey, N., Ajo-Franklin, J., & Biondi, B. (2018). Introduction to interferometry of fiber optic strain measurements. EarthArXiv. Matsumoto, H., Araki, E., Kimura, T., Fujie, G., Shiraishi, K., Tonegawa, T., et al. (2021). Detection of hydroacoustic signals on a fiber-optic submarine cable. Scientific Reports, 11(1), 1–12. https://doi.org/10.1038/s41598-021-82093-8
- McMechan, G. A., & Yedlin, M. J. (1981). Analysis of dispersive waves by wave field transformation. *Geophysics*, 46(6), 869–874. https://doi.org/10.1190/1.1441225
- Mordret, A., Landès, M., Shapiro, N., Singh, S., Roux, P., & Barkved, O. (2013). Near-surface study at the valhall oil field from ambient noise surface wave tomography. *Geophysical Journal International*, 193(3), 1627–1643. https://doi.org/10.1093/gjji/ggt061
- NOAA. (2009). NOAA national geophysical data center. ETOPO1 1 arc-minute global relief model. NOAA National Centers for Environmental Information.
- Okal, E. A. (2008). The generation of T waves by earthquakes. Advances in Geophysics, 49, 1–65. https://doi.org/10.1016/s0065-2687(07)49001-x Posey, R., Jr., Johnson, G. A., & Vohra, S. T. (2000). Strain sensing based on coherent Rayleigh scattering in an optical fibre. Electronics Letters, 36(20), 1688–1689. https://doi.org/10.1049/el:20001200
- Ritzwoller, M. H., & Levshin, A. L. (2002). Estimating shallow shear velocities with marine multicomponent seismic data. *Geophysics*, 67(6), 1991–2004. https://doi.org/10.1190/1.1527099

SPICA ET AL. 10 of 11



- Rivet, D., de Cacqueray, B., Sladen, A., Roques, A., & Calbris, G. (2021). Preliminary assessment of ship detection and trajectory evaluation using distributed acoustic sensing on an optical fiber telecom cable. *Journal of the Acoustical Society of America*, 149(4), 2615–2627. https://doi.org/10.1121/10.0004129
- Sanchez-Sesma, F. J. (1987). Site effects on strong ground motion. Soil Dynamics and Earthquake Engineering, 6(2), 124–132. https://doi.org/10.1016/0267-7261(87)90022-4
- Sato, H., Fehler, M. C., & Maeda, T. (2012). Seismic wave propagation and scattering in the heterogeneous Earth (Vol. 496). Springer.
- Scholte, J. G. J. (1958). Rayleigh waves in isotropic and anistropic elastic media. Meded. Verhand. KNMI, 72, 9-43.
- Shinohara, M., Yamada, T., Akuhara, T., Mochizuki, K., Sakai, S., Hamakawa, M., et al. (2019). Distributed acoustic sensing measurement by using seafloor optical fiber cable system off Sanriku for seismic observation. In *Oceans 2019 MTS/IEEE Seattle* (pp. 1–4). Institute of Electrical and Electronics Engineers. https://doi.org/10.23919/oceans40490.2019.8962757
- Shinohara, M., Yamada, T., Sakai, S., Shiobara, H., & Kanazawa, T. (2016). Development and installation of new seafloor cabled seismic and tsunami observation system using ICT. In *Oceans 2016 MTS/IEEE Monterey* (pp. 1–4). Institute of Electrical and Electronics Engineers. https://doi.org/10.1109/oceans.2016.7761350
- Singh, S., Capdeville, Y., & Igel, H. (2020). Correcting wavefield gradients for the effects of local small-scale heterogeneities. Geophysical Journal International, 220(2), 996–1011.
- Sladen, A., Rivet, D., Ampuero, J. P., De Barros, L., Hello, Y., Calbris, G., & Lamare, P. (2019). Distributed sensing of earthquakes and ocean-solid earth interactions on seafloor telecom cables. *Nature Communications*, 10(1), 1–8, https://doi.org/10.1038/s41467-019-13793-z
- Spica, Z., Perton, M., Nakata, N., Liu, X., & Beroza, G. C. (2018). Shallow V_s imaging of the Groningen area from joint inversion of multimode surface waves and H/V spectral ratios. Seismological Research Letters, 89(5), 1720–1729. https://doi.org/10.1785/0220180060
- Spica, Z. J., Nishida, K., Akuhara, T., Pétrélis, F., Shinohara, M., & Yamada, T. (2020). Marine sediment characterized by ocean-bottom fiber-optic seismology. *Geophysical Research Letters*, 47(16), e2020GL088360. https://doi.org/10.1029/2020gl088360
- Spica, Z. J., Perton, M., Martin, E. R., Beroza, G. C., & Biondi, B. (2020). Urban seismic site characterization by fiber-optic seismology. *Journal of Geophysical Research: Solid Earth*, 125(3), e2019JB018656. https://doi.org/10.1029/2019jb018656
- Talandier, J., & Okal, E. A. (1998). On the mechanism of conversion of seismic waves to and from T waves in the vicinity of island shores. *Bulletin of the Seismological Society of America*, 88(2), 621–632, https://doi.org/10.1785/BSSA0880020621
- Taweesintananon, K., Landrø, M., Brenne, J. K., & Haukanes, A. (2021). Distributed acoustic sensing for near surface imaging from submarine telecommunication cable: Case study in the Trondheim Fiord.
- Tonegawa, T., Fukao, Y., Takahashi, T., Obana, K., Kodaira, S., & Kaneda, Y. (2015). Ambient seafloor noise excited by earthquakes in the Nankai subduction zone. *Nature Communications*, 6(1), 6132. https://doi.org/10.1038/ncomms7132
- van den Ende, M., & Ampuero, J.-P. (2021). Evaluating seismic beamforming capabilities of distributed acoustic sensing arrays. *Solid Earth*,
- 12(4), 915–934. https://doi.org/10.5194/se-12-915-2021 Wessel, P., Luis, J., Uieda, L., Scharroo, R., Wobbe, F., Smith, W., & Tian, D. (2019). The generic mapping tools version 6. *Geochemistry, Geo-*
- physics, Geosystems, 20(11), 5556–5564. https://doi.org/10.1029/2019gc008515 Williams, E. F., Fernández-Ruiz, M. R., Magalhaes, R., Vanthillo, R., Zhan, Z., González-Herráez, M., & Martins, H. F. (2019). Distributed sensing
- of microseisms and teleseisms with submarine dark fibers. *Nature Communications*, 10(1), 1–11. https://doi.org/10.1038/s41467-019-13262-7 Williams, E. F., Fernández-Ruiz, M. R., Magalhaes, R., Vanthillo, R., Zhan, Z., González-Herráez, M., & Martins, H. F. (2021). Scholte wave inversion and passive source imaging with ocean-bottom DAS. *The Leading Edge*, 40(8), 576–583. https://doi.org/10.1190/tle40080576.1
- Yuan, S., Lellouch, A., Clapp, R. G., & Biondi, B. (2020). Near-surface characterization using a roadside distributed acoustic sensing array. The Leading Edge, 39(9), 646–653, https://doi.org/10.1190/tle39090646.1
- Yue, H., Castellanos, J. C., Yu, C., Meng, L., & Zhan, Z. (2017). Localized water reverberation phases and its impact on backprojection images. Geophysical Research Letters, 44(19), 9573–9580. https://doi.org/10.1002/2017gl073254
- Zhan, Z. (2020). Distributed acoustic sensing turns fiber-optic cables into sensitive seismic antennas. Seismological Research Letters, 91(1), 1–15. https://doi.org/10.1785/0220190112
- Zheng, Y., Fang, X., Liu, J., & Fehler, M. C. (2013). Scholte waves generated by seafloor topography. arXiv preprint arXiv:1306.4383.
- Zhu, J., & Popovics, J. S. (2006). Analytical study of excitation and measurement of fluid-solid interface waves. *Geophysical Research Letters*, 33(9). https://doi.org/10.1029/2006g1026068

Reference From the Supporting Information

Hayes, G., Moore, G., Portner, D., Hearne, M., Flamme, H., Furtney, M., & Smoczyk, G. (2014). Slab2, a comprehensive subduction zone geometry model. Science, 6410(362), 58–61.

SPICA ET AL.